Elaboration of Controlled Structure Foams with the SMX Static Mixer

Emeline Talansier
GEPEA-UMR-CNRS 6144, Oniris site Géraudière, BP 82225, F-44322 Nantes Cedex 3, France

Dominique Dellavalle
LTN-UMR-CNRS 6602, Oniris site Géraudière, BP 82225, F-44322 Nantes Cedex 3, France

Catherine Loisel and Anne Desrumaux
GEPEA-UMR-CNRS 6144, Oniris site Géraudière, BP 82225, F-44322 Nantes Cedex 3, France

Jack Legrand
LUNAM Université, Université de Nantes, CNRS, GEPEA, UMR 6144, CRTT, BP 420F-44500 St-Nazaire, France

DOI 10.1002/aic.13796
Published online April 16, 2012 in Wiley Online Library (wileyonlinelibrary.com).

A better control of the foaming process is important for food industry, as the structure of the liquid/gas mixture is a key parameter for the end-used properties of foams. The main concern of this study is to present a methodology applicable to the parametric study of the foaming process that can help either to optimize the operating conditions or to adapt the formulation. We focused on the valorization of egg white proteins (EWPs). The method allows studying the effect of the process parameters on the foam structure and the effect of the thermal pretreatment of the EWP in the dry state on the rheology and the stability of foams. The foaming is achieved with a SMX10 static mixer, which allows the production of controlled structure foams. It is, therefore, possible to investigate the dependence of foam properties by comparing foams with the same alveolar structure in relation with their formulation. © 2012 American Institute of Chemical Engineers *AIChE J,* 59: 132–145, 2013
Keywords: foam, food, process control, mixing, rheology

Introduction

Food foams represent a large variety of aerated products including dairy foams, meringues, meat foams, or confectionary products of increasing importance for consumers. They offer a lighter texture with improved spreadability, among a large variety of tastes and nutritional allegations.[1] Food foams may be considered as ''solid'' (like meringue) or ''liquid'' (whipped cream, beaten egg whites) depending on the rheological properties of the continuous phase. The stability of liquid foams is ensured by functional ingredients: the proteins and the hydrocolloids, acting as surface-active agents and texturizers of the matrix, respectively. Compared to other proteins (particularly the whey protein isolates), the egg white proteins (EWPs) offer denser and more stable foams[2] with the disadvantage of being more expensive. Heat treatment of egg white powder is performed in the industry with the double effect of pasteurization and improvement of the functional properties.[3–5] The influence of the formulation on the stability and texture of food foams has been extensively studied particularly in dairy desserts,[6,7] but the contribution of the structural properties, namely air content and bubble size distribution, on the foam behavior is still unclear.

The foaming process consists in dispersing a gas in a liquid matrix, before any further treatment like cooking or conditioning. The gas mixing may be achieved by batch whipping, as for traditional whipped cream. However, the air content entrapped during foaming is not controlled under these conditions, leading to a lack of reproducibility. Continuous processes are sometimes preferred by food manufacturers, like scraped surface heat exchangers for ice cream process,[8,9] or cogged rotor-stator units, like the well-known Mondomix™ [9–14] for a better control of the holdup. Nevertheless, the development of such processes is not straightforward. Numerous parameters, such as the gas and liquid flow rates, the design and the speed of the whipping head, the backpressure and the temperature, have to be fitted to the physicochemical properties of the mix (viscosity and shear resistance) to obtain the desired foam characteristics.[15–20]

Static mixers are widely used in various industrial processes[21–23] and notably for liquid–liquid[24–28] or gas–liquid[29–33] dispersion. They offer a promising alternative to the rotor-stator foaming devices in terms of maintenance (no rotating pieces), compactedness, homogeneous shearing, and energy saving.[23,25,34–36] The pumping energy in static mixers is more efficiently redistributed between mixing and fluid momentum than in batch stirring equipments. Nevertheless, some

Correspondence concerning this article should be addressed to E. Talansier at etalansier@gmail.com.

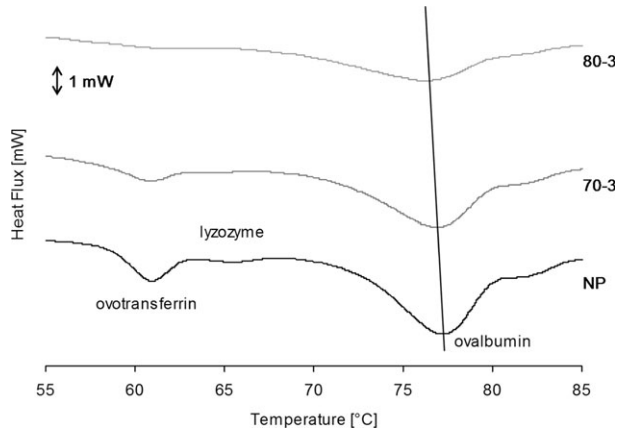

Figure 1. Typical thermograms obtained with EWP solutions at 12.5% (w/w) for NP, 70-3 and 80-3 heat treatment conditions.

The heating rate is 0.5°C/min.

limitations can occur due to the transitions of hydrodynamic regimes, depending on the gas and liquid flow rates: the two phases may remain segregated in slug flow or stratified regimes. To get a good mixing, the dispersed bubbles regime is the only convenient one. Generally, this regime relies on two criteria: a sufficient strain rate induced by the flow, and a moderate gas volume fraction, conditions that are fulfilled for all the operating conditions presented here. Actually, the dispersed regime domain is much wider for the static mixer than for the empty pipe, and moreover favored by the surface-acting properties of the egg white.

The main purpose of this study is to demonstrate that static mixers, in this case the SMX10 (Sulzer^{TM}, 25 elements) are suitable in a certain extent to produce foams of controlled structural aspect, that are bubble size distribution and void fraction. In conventional processes, the formulation strongly influences the foam structure so that it is difficult to discriminate between the two effects. From this point of view, open loop system has some advantages because the void fraction is perfectly determined by the flow rates, under the condition that the gas is perfectly mixed in the liquid matrix. That is not the case in all the processes, for example, a 30–80% gas incorporation efficiency is commonly encountered in the Mondomix,[17–19] situation that makes impossible any theoretical prediction or mastering of the overrun. The SMX10^{TM} is chosen here for its ability of providing a fully dispersed hydrodynamic regime in a wide range of flow rates. Similar study could be carried out with any other apparatus allowing a "perfect" mixing in a wide range of operating conditions (sufficient and homogeneous shearing, quasi plug flow). At this condition, the foam properties for a given L/G system can be linked to the structure, and conversely, different formulations of the liquid phase in the foam can be compared with an identical structure. The limitation on the latter point is that the different liquid solutions to be compared must present the same L/G interfacial tension, to ensure the same capillary number, and finally the same bubble diameter. This condition is fulfilled with the different EWP solutions that have to be characterized in our study, and the influence of the different parameter can be better understood and quantified. This methodology is ought to be carried out with another type of mixing system and foam liquid bases that fulfill the precited criteria.

The material and the experimental equipment, including the characterization methods, are presented in the section entitled Materials and Methods. In the section entitled Foam structuration with the SMX Static Mixer, a wide range of flow rates is tested to investigate the effect of the operating conditions on the foam structure with various solutions. The dependence of the end-used properties of the foams—mainly texture and stability—on the EWP denaturation is presented in the section entitled Effect of the Structure and of the Liquid Matrix on the End-Used Properties of Foam. Based on pressure drop data, an estimate of the in-line viscosity is attempted in the section entitled Pressure Drop and Process Viscosity.

Materials and Methods

EWP solutions

Solutions Preparation. EWPs powder, elaborated by spray drying of fresh egg white, was purchased from the Igreca Company (Seiches sur le Loir 49, France). In this state, the proteins have yet undergone a certain denaturation, but no posterior heat treatment, so that the samples are named "NP" and constitute the "zero" reference. Some batches are submitted to different time-temperature conditions (70–80°C, 1–3 days) in an oven VÖTSCH^{TM} VC 7018; they are named *x–y*, where *x* is the oven temperature and *y* is the number of days.

The powders were rehydrated with tap water at a protein concentration of 12.5% (w/w) (or 143 g/L). A full description of the methods is available in Talansier et al.[37,38]

Differential Scanning Calorimetry. Differential scanning calorimetry (DSC) is the appropriate tool to observe the effect of the heat treatment on the protein denaturation. DSC curves were performed by using a microcalorimeter (SETARAM, micro DSC III, France). Typical thermograms for each heat treatment condition are represented in Figure 1. They exhibit three visible peaks, around 60, 65, and 80°C, corresponding to the denaturation of ovotransferrin, ovalbumin, and lysozyme, respectively. The increase in the intensity of the preheating treatment clearly appears in DSC profiles. It leads to a gradual broadening and a decrease of the peaks, as well as a shift of the peak temperature to lower values.

Surface Tension. The surface tension was measured using the pending drop method (Interfacial Technology Concept^{TM}, Longessaigne, France). The image of an air bubble formed at the tip of a capillary connected with a syringe is taken

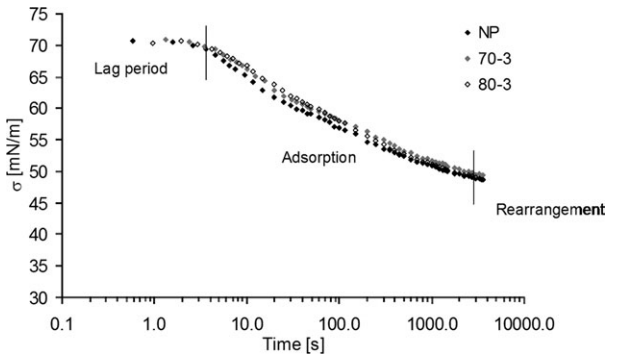

Figure 2. The adsorption kinetics of EWP at the air/liquid interface for the NP, 70-3 and 80-3 conditions.

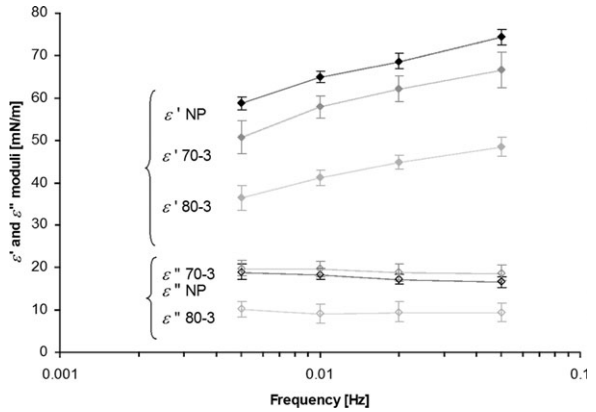

Figure 3. Interfacial mechanical spectra for the NP, 70-3 and 80-3 solutions.

Table 1. Properties of EWP Solutions for the Different Heat Treatment of EWP Powders

Denaturation Conditions	NP	70-3	80-3
η (Pa s) $\pm$ 0.06%	0.008	0.008	0.008
σ_{eq} (mN m^{-1}) $\pm$ 3%	49.1	49.5	47.6
$\lvert\varepsilon^*\rvert_{0.01Hz}$ (mN m^{-1}) $\pm$ 5%	67.6	61.2	42.3

from a CCD camera and digitalized. The surface tension σ (N m^{-1}) is computed by analyzing the contour of the bubble according to the Laplace–Young equation. The evolution of the surface tension was observed as function of time over 3600 s, duration at which the equilibrium value σ_{eq} is supposed to be reached. The shape of the curve (Figure 2) is consistent with the literature concerning the protein solutions.[39] The slope changes reflect physicochemical phenomena, especially the adsorption kinetics of the proteins at the interface for the middle part. The main conclusion is that the three formulations do not differ significantly, as the 3% decrease from NP to 80-3 observed for σ_{eq} is within the 5% measurement reproducibility.

Interfacial Rheology. The EWP solution is diluted to 1/100 factor, and the measurements of the bubble interface dilatational elasticity are performed when the protein adsorption is completed in the static step during the surface tension measurements, with the same device in the dynamic mode (I.T. Concept, France). A 6 μL air bubble is formed upward at the tip of a U-shaped stainless steel needle immersed in a vessel filled with the protein solution under gentle stirring. The system temperature is maintained at 20 $\pm$ 0.1°C.

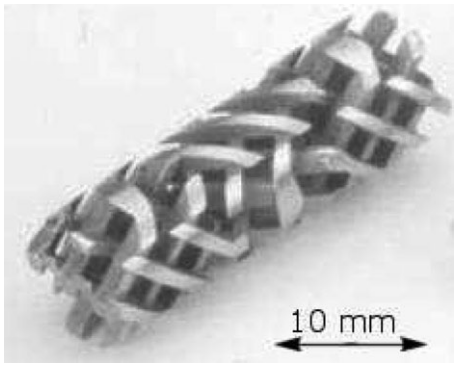

Figure 5. Element of SMX10 Sulzer™ geometry.

Pulsations of the syringe are controlled by a stepping motor for application of a sinusoidal drop volume inducing a periodic drop surface dilatational strain of 6.25% (reported to the surface) in the (0.005–0.05 Hz) frequency range. The strain amplitude was chosen to lay in the linearity of the dilatational moduli, according to previous studies[40,41] on protein solutions in the same concentration range (0.01–0.001%).

It can be observed on the mechanical spectra (Figure 3) that the denaturation has a significant effect on the interfacial viscoelasticity: as the heat treatment is more intense, the elastic modulus decreases. The modulus $|\varepsilon^*|$ at the frequency of 0.01 Hz, namely $|\varepsilon^*|_{0.01Hz}$ is chosen as the characteristic parameter, and its values are gathered with the other physical properties in Table 1.

Viscosity. The flow curves of the egg white solution (Figure 4) were carried out with a Couette system on the AR1000-N Rheolyst rheometer (TA Instruments™, France), in the (60–200 s^{-1}) shear rate range. It clearly appears that EWP solutions are Newtonian and present viscosity values around 0.008 Pa s at 20°C, whatever the heat treatment.

Summary of the Physical Properties of EWP Solutions. The viscosity, the surface tension, and the interfacial modulus are summarized in Table 1 as a function of the thermal treatment. Noteworthy, the thermal denaturation has no significant influence on the viscosity and on the surface tension, but only modifies the interfacial rheology.

SMX10 static mixer

Principle. The SMX, as seen in Figure 5, consists in an insert[42] made of alternate blades that generates a mixing by the division and recombination of the stream lines, as a "comb sweep" on the static volume, alternatively in one direction and the perpendicular one, generating a periodical

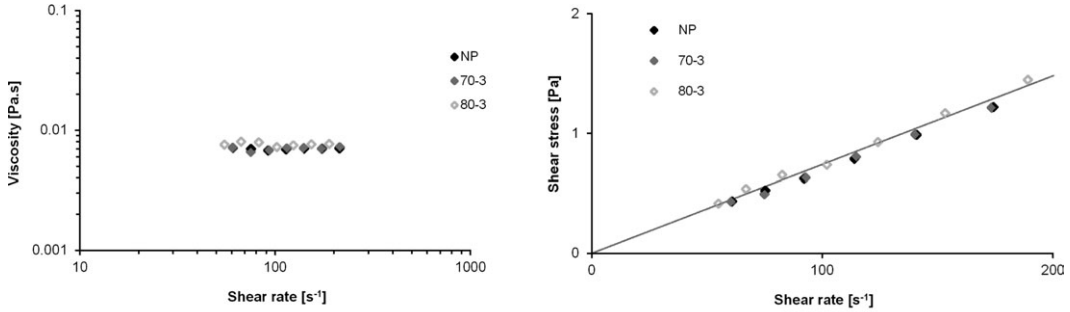

Figure 4. Flow curves for the heat-treated EWP solutions NP, 70-3 and 80-3 EWP solutions.

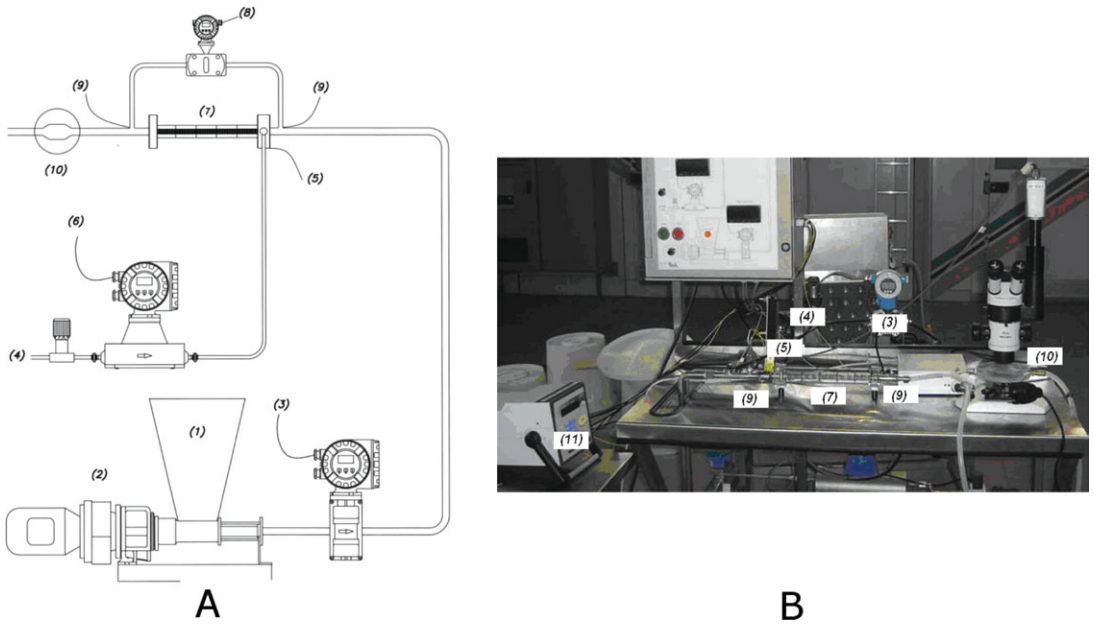

Figure 6. A & B Experimental rig (1) liquid feed; (2) pump; (3) volumetric liquid flow meter; (4) air injection; (5) absolute air pressure sensor before injection dye; (6) mass air flow meter; (7) static mixer; (8) differential pressure sensor; (9) temperature sensors; (10) visualization cell for image analysis; (11) data acquisition system.

[Color figure can be viewed in the online issue, which is available at wileyonlinelibrary.com.]

striation. A high shear rate results from the small hydraulic diameter[42] and a stretching effect is induced by the curvature of the streamlines.

For multiphase applications, like emulsification and foaming, the inner phase is injected in the main flow, and the volume fraction of the mixture, in the dispersed regime, is fixed by the local volume flow rates, Q_D for the dispersed phase and Q_C.

$$\alpha_{local} = \frac{[Q_D]_{local}}{[Q_C]_{local} + [Q_C]_{local}} \quad (1)$$

In foaming process, the liquid volume flow rate is constant in all the cross-sections of the reactor, while the gas volume flow rate depends on the local pressure. Hence, conversely to other mixing processes like emulsification, the in-line foaming never reaches an "equilibrium state" along the mixer. Actually, the gas bubbles continuously expand along the static mixer under the pressure drop, while the velocities and the strain rates increase thereby enhancing the break-up. This feature must be taken into account in the design of the process.

Hydraulic Loop. The static mixer SMX10 Sulzer™ with 25 elements is included in the hydraulic loop presented in Figure 6. Details of the static mixer geometry are given in Table 2. The test section is fed by the liquid phase stored in the hopper, and by the compressed air delivered at the inlet. Pressure sensors Ceraphant T and Deltabar S (Endress+Hausser™) are located at the gas inlet and at the bounds of the test section to measure the pressure drop. Liquid and gas mass flow rates are monitored by flow meters Proline Promag 50 and Promass 80 (Endress+Hausser™). A part of the foam flux is by-passed to a visualization cell.

Table 2. Size of the Elements of the SMX10 Sulzer™ Static Mixer

Parameter	Symbol	Value
Number of elements	n	25
Total length	L	0.25 m
Pipe diameter	D	0.010 m
Hydraulic diameter	D_H	0.00265 m
Porosity	ε	0.77

Air Injection System. A specific geometry has been designed for the air injection into the main liquid. In the view to improve the mixing (and, thus, reduce the mixer length), the gas is introduced by an annular dispenser with 12 tubular holes symmetrically located around the section, as seen in Figure 7.

Foam properties and characterization parameters

Overrun. The overrun is practically determined by weighting a given volume of foam

$$\mathrm{OV}(\%) = 100 \times \frac{(\text{wt 100mL solution}) - (\text{wt 100mL foam})}{(\text{wt 100mL foam})} \quad (2)$$

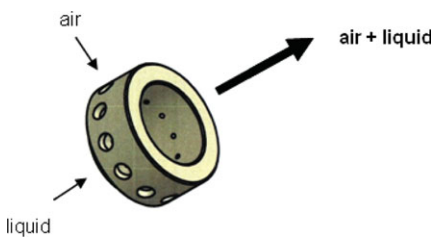

Figure 7. Air injection geometry.

[Color figure can be viewed in the online issue, which is available at wileyonlinelibrary.com.]

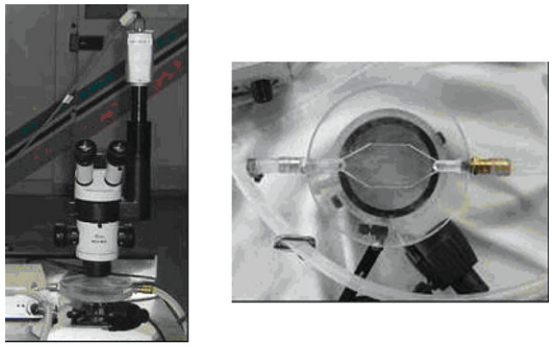

A B

Figure 8. A.On-line picture acquisition system. B. Visualization cell.

[Color figure can be viewed in the online issue, which is available at wileyonlinelibrary.com.]

It is linked to the void fraction α by the relationship

$$\alpha = \frac{\mathrm{OV}(\%)}{100 + \mathrm{OV}(\%)} \tag{3}$$

Bubbles Size Distribution. Pictures of foam bubbles were taken on-line through a plane transparent visualization cell (Figure 8B) with a Digital Interface camera (DFW-SX910, Sony™,Japan) mounted on a Leica™ Stereozoom (Wild M3C) (Figure 8A). The image analysis, carried out with the software Visilog2.0™ (Noesis), provided the experimental values of bubbles size distribution under the pressure of the visualization cell P_{cell}. A least six pictures were analyzed, meaning a series of approximately 1000 bubbles for one run. This was considered as sufficient to converge to the true probability density function (pdf).[43]

To make the results more tractable, we have attempted to fit a statistic law to the experimental distribution. As shown on Figure 9A, the normal law fairly fits the pdf, whereas the lognormal law appears not suitable. The modal diameter and the standard deviation of the normal law modeling were computed from the experimental diameter series. In the frequency distribution, the modal diameter is simply the linear mean of the series. The Figure 9B shows an example of various bubble size distributions fitted with the normal law, obtained at increasing flow rates from right to left, for a given void fraction ($\alpha = 0.92$).

The modal diameter D_{mC} is determined in the cell section, which is under pressure; the gas expansion till the outlet is accounted for following the perfect gas law, so that the corresponding value D_{mA} at ambient is

$$D_{\mathrm{mA}} = D_{\mathrm{mC}} \left(\frac{P_{\mathrm{cell}}}{P_{\mathrm{atm}}} \right)^{1/3} \tag{4}$$

In this correction, all the diameters are increased by a constant factor, thus the "shape" of the distribution is not modified: the dispersion factor, ratio of the standard deviation by the modal diameter, is not changed by the expansion.

Foam Rheology. Measurements are performed using a stress-controlled rheometer (AR1000-N Rheolyst, TA Instruments™, France) equipped with a Peltier circulator for temperature control, at 4°C in the present case. A specific protocol was developed to ensure linearity of the measurements, minimize the wall slip, and preserve the foam structure.

An identical gap of 2.5 mm was used for all the measurements. A 2.5 mm gap value is considered as large enough to obtain representative foam samples (number of bubbles in the cross-section $\gg 10$) and reduce the shear layer phenomena (defect lines in the sample), and small enough for an accurate shear rate determination. The linear regime was investigated in the (0.05–5)% strain range (Figure 10A). The 0.5% oscillation amplitude was chosen as the best compromise toward the linear domain and the limits of the rheometer sensor. A cross-hatched surface was compared to a stainless-steel one for the upper plate (Figure 10A) to evaluate the wall slip effects. The profiles are systematically lower with the rough surface, proving that the foams present a sufficient adhesion to the upper plate and that the stainless-plate seems appropriate for relevant measurements; even though they cannot be considered as absolute values considering the complexity of the foam behavior, due to the bubbles rearrangement under very low deformation. Actually, it might also be sensitive to the loading procedure, which is carried out with the concern to minimize the strain: a thin fresh foam layer is carefully poured with a spatula onto the base

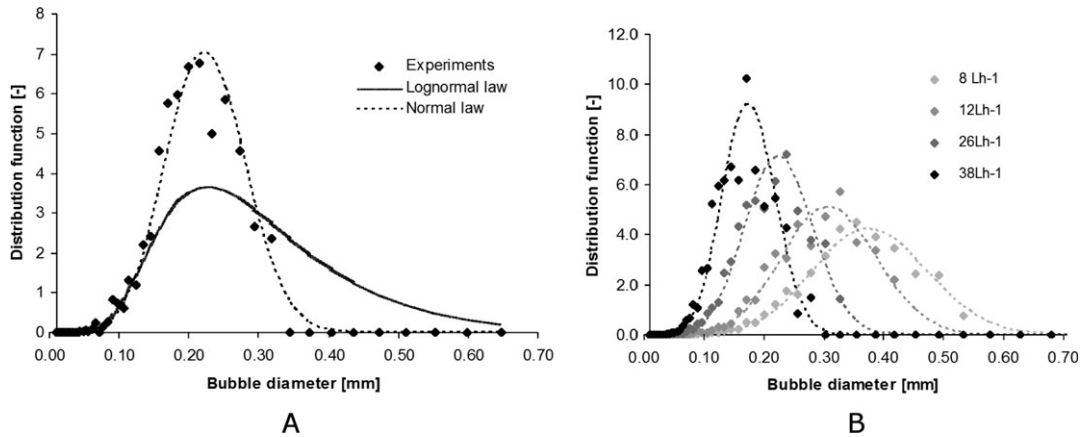

A B

Figure 9. Bubbles size pdf volume distribution.

A. Determination of the appropriate distribution law. B. Effect of the flow rate at the same void fraction ($\alpha = 0.92$) for the NP, fitted with the normal law.

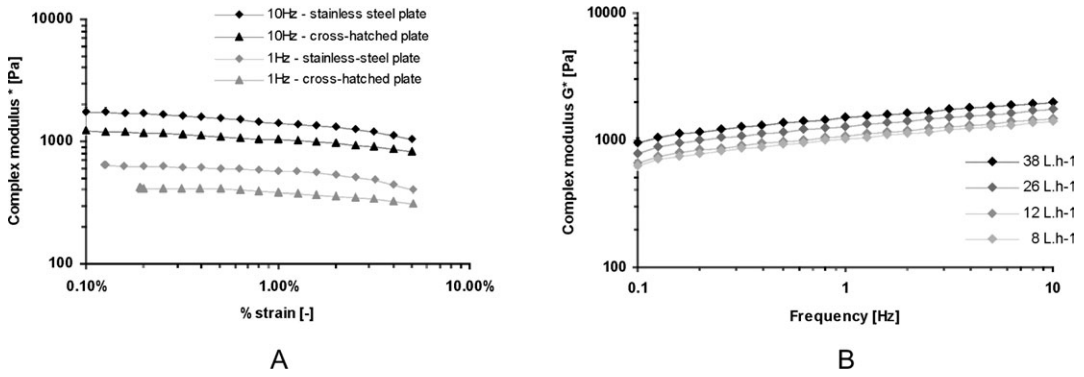

Figure 10. Foam rheology.

A. Determination of the linear regime at 1 and 10 Hz using stainless-steel plate and cross-hatched plate. B. Examples of mechanical spectra for the NP, $\alpha = 0.92$, at various liquid flow rates (8,12,26 and 38 L h^{-1}) carried out with stainless-steel plate.

plate cooled at 4°C. Then, the upper plate is lowered to the nominal gap.

In these conditions, mechanical spectra (Figure 10B), performed in the 0.1–10 Hz frequency sweep, were shown to be fairly repeatable (less than 5% standard deviation) and reproducible with an 8% accuracy (Tables 3–5). The viscoelastic modulus |G*| at 1 Hz is chosen as the characteristic parameter of the foam rheology.

Foam Stability. The container filled up for the overrun measurement was turned upside down and placed on a balance. The weight of drained liquid was recorded over 180 min. Experimental profiles of liquid drainage were shown in Figure 11. The lag period before the first drop, t_0, corresponds to the mean of the three samples and is proposed here as the criterion of foam stability.

Foam Structuration with the SMX Static Mixer

Design of the experiments

In the open loop foaming process, the couple of liquid/gas mass flow rates fully determines the foam conformation at the outlet, for a given composition of the liquid phase.

The void fraction is given by Eq. 5 in the dispersed regime, when the gas is entirely trapped in the liquid matrix.

Table 3. Effect of Process Conditions on Foam Structure and End-Used-Properties – NP liquid base

	Q_L (L h^{-1})	10	12	16	21	26	32	38	45
α	Q_{Gm} (Kg h^{-1})	–	–	–	0.400	–	–	–	–
0.94	P_I (Pa)	–	–	–	277,071	–	–	–	–
	ΔP (Pa)	–	–	–	97,464	–	–	–	–
	D_{mA} (μm)	–	–	–	178	–	–	–	–
	DI (−)	–	–	–	0.354	–	–	–	–
	t_0 (s)	–	–	–	5433	–	–	–	–
	$\|G^*\|_{1Hz}$ (Pa)	–	–	–	1890	–	–	–	–
	Q_{Gm} (Kg h^{-1})	0.137	0.162	0.224	0.285	0.353	0.441	0.516	0.598
0.92	P_I (Pa)	188,858	199,998	214,934	232,258	252,269	273,015	287,447	309,645
	ΔP (Pa)	51,264	51,407	66,300	69,400	89,158	95,000	109,122	123,062
	D_{mA} (μm)	302	258	231	208	202	187	154	152
	DI (−)	0.350	0.381	0.373	0.392	0.362	0.361	0.366	0.360
	t_0 (s)	–	1667	1917	1733	–	3153	3377	2947
	$\|G^*\|_{1Hz}$ (Pa)	1029	1086	1230	1251	1291	1511	1441	1615
	Q_{Gm} (Kg h^{-1})	0.110	0.132	0.168	0.227	0.276	0.352	0.402	0.525
0.90	P_I (Pa)	174,376	180,609	189,127	203,039	222,478	241,988	255,552	294,442
	ΔP (Pa)	42,118	44,833	54,439	67,826	72,219	84,369	97,114	117,000
	D_{mA} (μm)	341	292	286	247	233	220	182	149
	DI (−)	0.372	0.374	0.348	0.384	0.380	0.372	0.390	0.429
	t_0 (s)	280	290	470	532	850	1420	1645	
	$\|G^*\|_{1Hz}$ (Pa)	884	946	905	1086	1054	1192	1132	1490
	Q_{Gm} (Kg h^{-1})	0.089	0.111	0.145	0.191	0.233	0.286	0.337	0.397
0.88	P_I (Pa)	160,192	171,897	179,646	187,992	206,272	222,009	231,556	246,378
	ΔP (Pa)	36,352	38,118	43,585	53,800	64,115	80,767	80,767	91,310
	D_{mA} (μm)	368	362	321	268	250	234	205	184
	DI (−)	0.362	0.348	0.358	0.400	0.374	0.381	0.391	0.388
	t_0 (s)	170	210	280	230	590	370	460	735
	$\|G^*\|_{1Hz}$ (Pa)	749	842	789	898	921	1064	1001	1023
	Q_{Gm} (Kg h^{-1})	0.071	–	0.112	0.144	–	0.217	–	0.305
0.85	P_I (Pa)	144,093	–	162,628	170,284	–	196,178	–	218,335
	ΔP (Pa)	–	–	40,900	47,534	–	58,573	–	77,976
	D_{mA} (μm)	408	–	342	280	–	240	–	207
	DI (−)	0.364	–	0.323	0.319	–	0.372	–	0.398
	t_0 (s)	–	–	–	–	–	–	–	–
	$\|G^*\|_{1Hz}$ (Pa)	–	–	675	–	–	786	–	892

% error D_{mA} (μm) 8%; DI (−) 8%; $|G^*|_{1Hz}$ (Pa) 8%; t_0 (s) 18%.

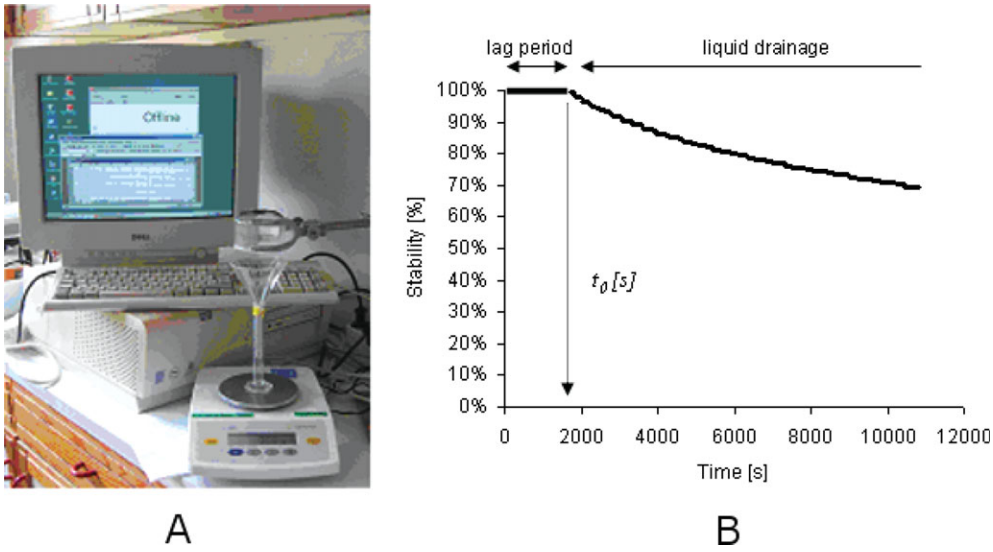

Figure 11. Stability curves.

A. Experimental set-up and recording of liquid weight. B. Example of stability curve obtained for the NP,$\alpha = 0.92$, $Q_L = 8$ L h^{-1} condition. [Color figure can be viewed in the online issue, which is available at wileyonlinelibrary.com.]

$$\alpha_{\text{theoretical}} = \frac{Q_{Gm}/\rho_{G,atm}}{Q_{Gm}/\rho_{G,atm} + Q_L} \quad (5)$$

with Q_L the liquid volume flow rate, Q_{Gm} the gas mass flow rate, and ρ_{Gatm} the gas density at ambient. In this definition, it can be observed that the final void fraction only depends on the gas mass flow rate, but neither on the injection pressure nor on the fluid properties. The bubble diameter on the contrary also depends on the fluid properties, and, thus, is not a straightforward function of the flow rates. Actually, as all the solutions present the same viscosity and surface tension that constitute the governing parameters for the break-up process. Hence, one can expect that the foam structure at the outlet of the device will not be affected by the EWP denaturation. The purpose of this section is to establish that the foam structure is determined by the operating conditions, and that this structure is not modified by the heat treatment of the EWPs in the different liquid solutions. Three series of experiments are designed to assess the foam structuration:

1. effect of the liquid flow rate and gas flow rates leading to given levels of void fractions at the outlet (0.85–0.94) for the NP liquid base (Table 3),

2. sweep of gas flow rates at a given liquid flow rate ($Q_L = 21$ L h^{-1}) for the NP, 70-3 and 80-3 solutions (Table 4),

3. sweep of liquid/gas flow rates couples leading to the $\alpha = 0.92$ void fraction at the outlet, for the NP, 70-3 and 80-3 solutions (Table 3).

The resulting size distribution is given in the tables according to the parameters of the normal law, which are the modal diameter at ambient (D_{mA}) and the dispersion index *DI*, defined by the ratio of the bubble size distribution standard deviation by the modal diameter. Rheological properties and stability of foams are then exploited in the section entitled Effect of the Structure and of the Liquid Matrix on the End-Used Properties of Foam. Standard errors are indicated for each run series.

Table 4. Effect of Gas Flow Rate ($Q_L = 21$ L h^{-1})

Q_L (L h^{-1})				21		
Q_{Gm} (Kg h^{-1})		0.145	0.182	0.225	0.285	0.400
α (−)		0.85	0.88	0.90	0.92	0.94
NP	P_I (Pa)	170,284	187,991	203,038	233,655	275,252
	ΔP (Pa)	47,534	53,800	64,942	73,450	97,464
	D_{mA} (μm)	280	268	247	212	178
	DI (−)	0.319	0.400	0.384	0.386	0.354
	t_0 (s)	–	230	532	1733	5433
	$\lvert G^*\rvert_{1Hz}$ (Pa)	–	898	1070	1310	1890
70-3	P_I (Pa)	178,326	195,862	212,778	240,547	279,425
	ΔP (Pa)	47,411	57,381	65,665	76,283	10,247
	D_{mA} (μm)	307	268	240	214	167
	DI (−)	0.375	0.363	0.368	0.369	0.381
	t_0 (s)	–	390	805	2410	7005
	$\lvert G^*\rvert_{1Hz}$ (Pa)	492	673	792	1003	1415
80-3	P_I (Pa)	178,667	197,220	213,082	245,029	281,049
	ΔP(Pa)	46,997	56,791	66,831	75,845	102,915
	D_{mA} (μm)	308	264	239	207	150
	DI (−)	0.373	0.373	0.380	0.340	0.359
	t_0 (s)	–	445	725	2330	5130
	$\lvert G^*\rvert_{1Hz}$ (Pa)	392	491	559	709	1013

% Error: D_{mA} (μm) 5%; DI (−) 9%; $\lvert G^*\rvert_{1Hz}$ (Pa) 9%; t_0 (s) 17%.

Table 5. Effect of Gas and Liquid Flow Rates at Constant Ratio $\alpha = 0.92$

Q_L (L h^{-1})		8	10	12	16	21	26	32	38	45
Q_{Gm} (kg h^{-1})		0.110	0.138	0.165	0.220	0.290	0.355	0.445	0.525	0.617
α (−)						0.92				
NP	P_I (Pa)	18,1128	18,7176	20,0105	21,5868	23,3875	25,1640	27,0255	28,8111	31,1291
	ΔP (Pa)	42,800	51,264	51,407	66,300	69,400	89,158	95,000	109,122	123,062
	D_{mA} (μm)	315	302	258	231	208	202	187	154	152
	DI (−)	0.365	0.350	0.381	0.373	0.392	0.362	0.361	0.366	0.360
	t_0 (s)	–	–	1667	1917	1733	–	3153	3377	2947
	$\lvert G^*\rvert_{1Hz}^{-}$ (Pa)	975	1029	1086	1230	1251	1291	1511	1441	1615
70-3	P_I (Pa)	–	193,763	201,232	218,830	240,206	259,963	281,473	297,355	297,355
	Δ(Pa)	–	48,114	53,797	65,866	77,460	90,450	100,988	108,306	120,935
	D_{mA} (μm)	–	275	261	233	214	187	162	159	140
	DI (−)	–	0.393	0.382	0.382	0.369	0.370	0.361	0.379	0.382
	t_0 (s)	–	–	1525	2933	2410	3408	3305	3513	3493
	$\lvert G^*\rvert_{1Hz}$ (Pa)	–	821	834	951	969	1012	1168	1205	1231
80-3	P_I (Pa)		206,656	224,765	245,057	260,467	26,046	282,756	306,184	323,054
	ΔP (Pa)			59,023	63,798	75,845	88,700	96,621	110,766	122,428
	D_{mA} (μm)	–	–	252	224	207	170	170	145	124
	DI (−)	–	–	0.365	0.367	0.340	0.367	0.361	0.367	0.377
	t_0 (s)	–	–	1285	1833	2330	2783	2848	3200	3440
	$\lvert G^*\rvert_{1Hz}$ (Pa)	–	–	586	661	698	749	775	808	899

% Error: D_{mA} (μm) 5%; DI (−) 8%; $\lvert G^*\rvert_{1Hz}$ (Pa) 8%; t_0 (s) 21%.

Control of the void fraction

For the whole of operating conditions (Tables 3–5), the measured void fraction is compared with the theoretical one in Figure 12, and it can be observed that the expected values are accurately reached. This shows that the gas is well mixed in the liquid phase without any leak.

Control of the bubble size

The typical bubble diameter results from a complex balance between the break-up, which is induced by the shear stress in the flow, the coalescence, linked to the collision probability (inversely proportional to the shear rate), and the gas expansion due to the pressure drop. A feedback effect of the bubble size on the viscosity and consequently the flow stresses renders a rigorous analysis of experimental data difficult.

Nevertheless, we have focused on the first-order effects, considering that the viscous and density effects remain lower than the shear rate one in the determination of the stress responsible for the break-up, in the experimental range of the study. Therefore, it is assumed that the kinematical effect of shearing is decisive for the bubble size, which is proportional to the resulting interstitial velocity U_E, which is the spanwise average of the velocity in the wet section of the SMX

$$U_E = U_L + U_{G,I} \tag{6}$$

with

$$U_L = \frac{Q_L}{S.\varepsilon} \tag{7}$$

and

$$U_{G,I} = \frac{Q_{Gm}}{S.\varepsilon.\rho_{G,I}} \tag{8}$$

The gas superficial velocity $U_{G,I}$ is arbitrarily taken at the gas injection (I). Actually, it is defined by the mass flow rate to its density at that point (known by the P_I experimental values in Tables 3–5).

All the diameters match a master curve, as presented in Figure 13 with a standard error of 5%, for all the products and the void fractions, confirming that the superficial velocity is a relevant scaling factor. The three points (circled on Figure 13) that lay relatively remote from the master curve

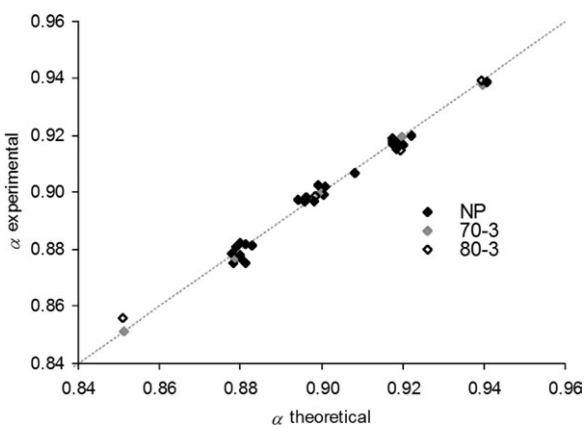

Figure 12. Control of the void fraction in the foaming process by the SMX static mixer.

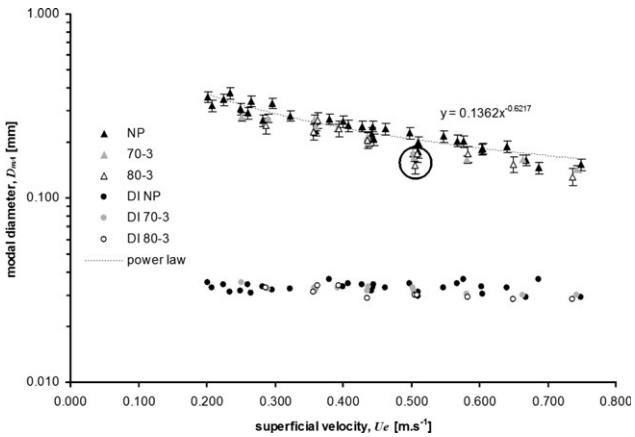

Figure 13. Control of the bubble diameter in the foaming process by the SMX static mixer.

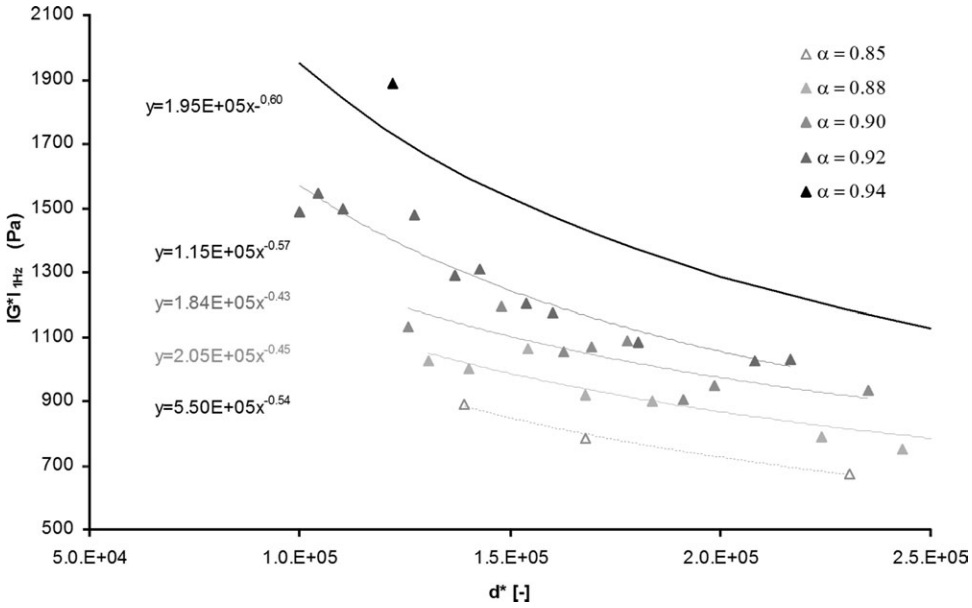

Figure 14. Influence of the bubble diameter on the foam texture—NP solution.

were obtained for the higher void fraction ($\alpha = 0.94$), where a bias is partly due to the underestimation of the reactor shear rate, which is taken at the inlet. The dispersion index *DI* remains constant, confirming the similarity of the granulometric profiles.

Effect of the Structure and of the Liquid Matrix on the End-Used Properties of Foam

Design of the experiments

The end-used properties of the foams—here the texture and the stability—basically depend on the overrun, the bubble size, the physical properties of the liquid matrix, and on the interfacial properties. With the experimental design presented in the section entitled Foam Structuration with the SMX Static Mixer, it is possible to investigate independently the influence of these parameters. First, considering a given liquid phase—NP in this case—the influence of the structure can be studied (Table 3). Second, the effect of the EWP denaturation on the foam properties will be explored considering foams of identical structure, at different void fraction (measured at ambient pressure: 0.85, 0.88, —0.90, and 0.92), and for the three liquid bases, NP, 70-3 and 80-3 (Tables 4 and 5).

Effect of the structure on the foam end-used properties (only NP)

As shown on Figure 14, at a given void fraction, the shear modulus of the foam strongly depends on the bubble diameter, as the trend curves give a nearly −0.6 power function (it is assumed that the same dependence is true for $\alpha = 0.94$). Likewise, at constant diameter, the foam firmness increases with the void fraction. According to the trend curves, this dependence is fitted by a −0.6 power function of $(1-\alpha)$ (Figure 15). This can be interpreted by physical considerations on the foam rheology. When the interfacial area become higher, the interfacial film is thinner and then the capillary forces take more importance, which means that the rheological behavior is less governed by the liquid phase properties and more by the interface properties.[44]

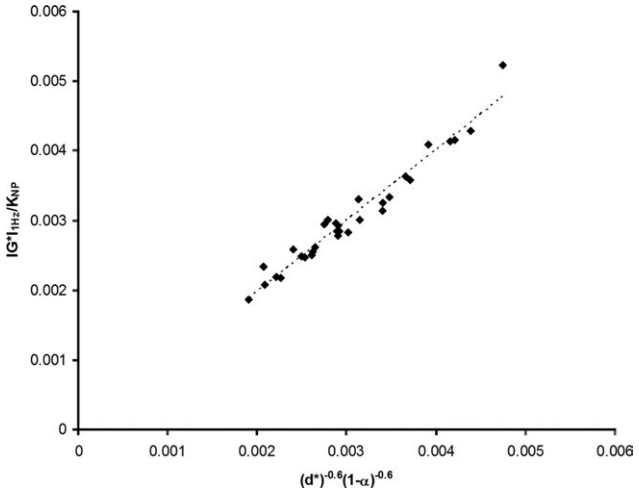

Figure 15. Comparison between experimental shear modulus $|G^*|_{1Hz}$—NP solution—and theoretical values derived from our model.

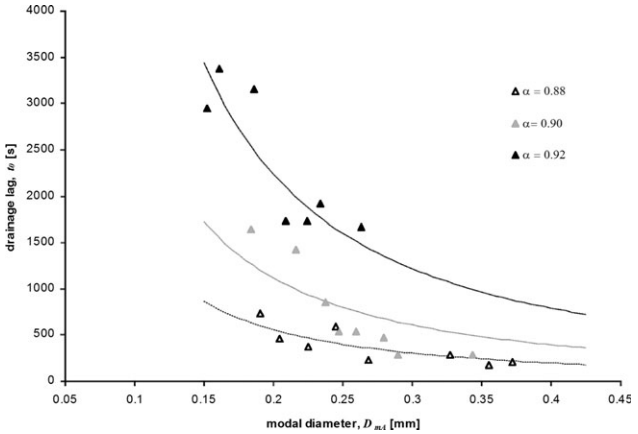

Figure 16. Influence of the bubble diameter on the foam stability—NP solution.

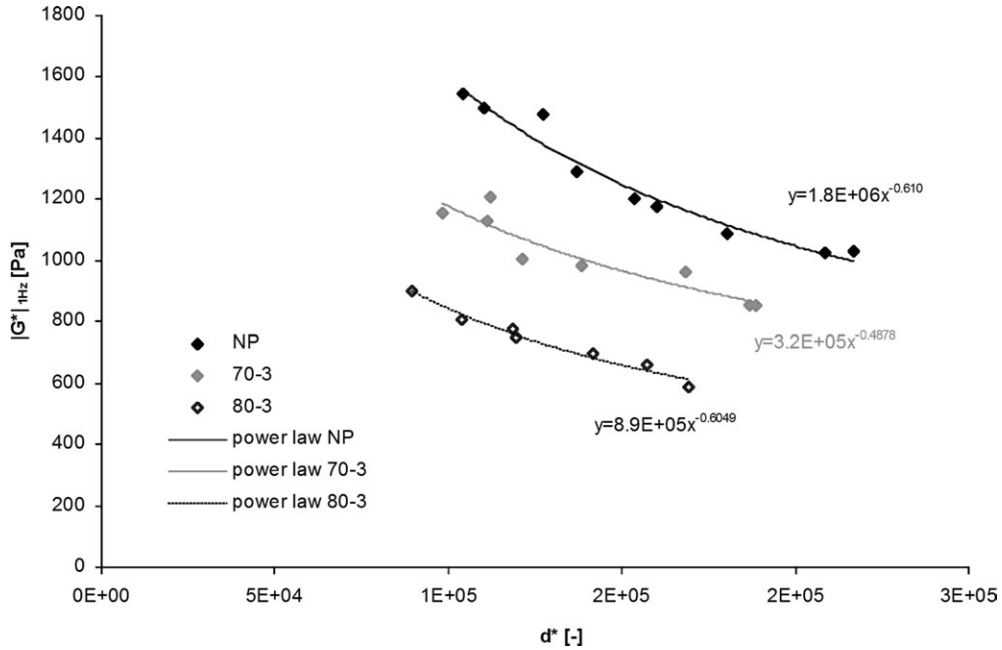

Figure 17. Influence of the denaturation on the foam texture—void fraction $\alpha = 0.92$.

Actually, the shear modulus can be modeled by a function of the two structure parameters of the foam that are the void fraction and the bubble diameter. The experimental data are fitted by the model presented in Eq. 10, involving the dimensionless diameter d^* defined in Eq. 9, where K_{NP} is a dimensionless constant relative to the NP liquid phase. Its adequacy with the experimental results is illustrated by Figure 15.

$$d* = \frac{D_{mA}.\sigma.\rho}{\eta^2} \tag{9}$$

$$|G^*|_{1hz} = K_{NP}(1-\alpha)^{-0.6} d*^{-0.6} \tag{10}$$

with $K_{NP} = 360{,}801$

The stability is also very sensitive to the foam structure. At the beginning of the drainage experience, the liquid phase cumulates at the sample bottom under gravity, by flowing in the interfacial film. The first drop falls when the local weight forces become larger than the holding forces, mainly the capillary and the viscous forces. As expected, the capillary forces are more intense for smaller bubbles. Concerning the viscous forces, they may increase inversely to the film thickness, one can refer for a simplistic approach to the Poiseuille law stating that the driving pressure (here the hydrostatic column) is a -4 power of the hydraulic diameter. These trends are confirmed in Figure 16, as it is observed first that the ''first drop lag,'' for three different void fractions in the range 0.88–0.92 sharply decreases when the bubble diameter increases (here fitted with a -1.5 power law), which means that the stability is improved by reducing the bubble size. The void fraction has also a significant effect on the stability; in our results, increasing of 0.02 point the void fraction leads approximately to duplicate the lag time. This can be interpreted as a direct consequence of the film thinning for higher void fractions.

Table 6. Texture Loss Factor due to the EWP Denaturation

k_{NP}	0%
$k_{70\text{-}3}$	25%
$k_{80\text{-}3}$	47%

Effect of EWP denaturation on the end-used properties of foams

The sets of operating conditions presented in the section entitled Foam Structuration with the SMX Static Mixer are now applied to investigate the effect of the nature of the liquid base. The properties of the foam are compared between samples presenting identical structures, as they have been processed under the same operating conditions—in the latter section we have noticed that the structure is determined by a given ''sum'' and ''ratio'' of the flow rates.

When considering the shear modulus in Figure 17, it appears that the foam texture is smoother for the most intense heat treatment. This is visible to the naked eye for the experimenter that the NP foam is more rigid and brittle, whereas the 70-3 and 80-3 present a more creamy aspect. The model suggested for NP (Eq. 10) is also applicable for the other liquid bases 70-3 and 80-3, where the constant K_{x-y} is specific for each product. The ''loss of texture factor''

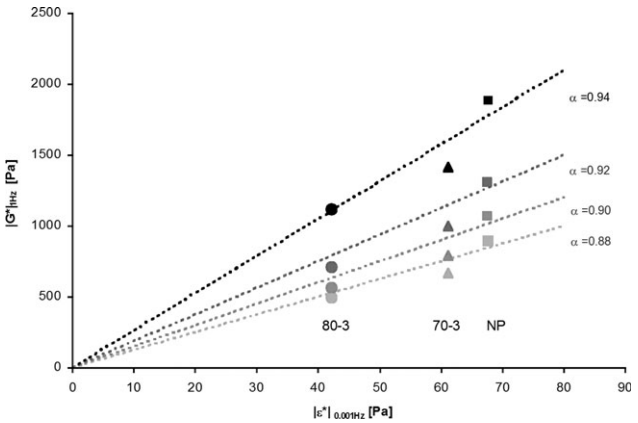

Figure 18. Effect of the interfacial elasticity on the foam texture.

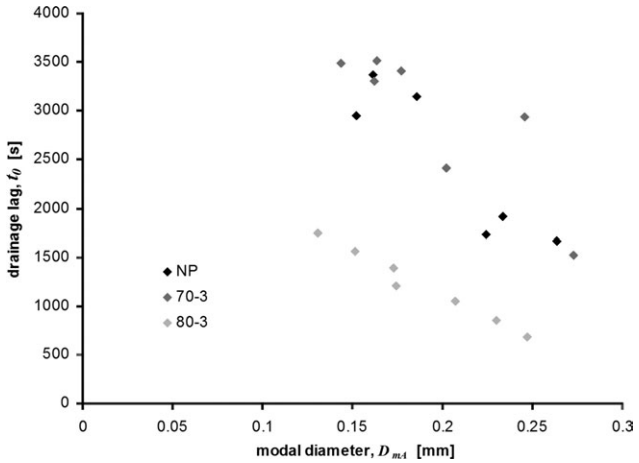

Figure 19. Influence of the EWP denaturation on the foam stability—void fraction α = 0.92.

k_{x-y} (%) (Table 6) can be defined by the ratio $(K_{NP}-K_{x-y})/K_{NP}$ to characterize the protein denaturation.

The dependence of the rheological behavior and the interfacial properties are shown in Figure 18, where the typical shear modulus is plotted versus the interfacial elongationnal modulus. Depending on the operating conditions, the points corresponding to the three products follow a linear trend, which means that for given alveolar structure, the shear modulus, or the "rigidity" of the foam seems nearly proportional to the interfacial elasticity.

The results concerning the stability—the first drop lag time—are presented in Figure 19 for samples with same void fraction, equal to 0.92. Beyond the main influence of the bubble diameter in the drainage process as discussed above, a second-order effect can be inferred with the bubble deformability. Actually the interface acts like a wall for the liquid flow in the interfacial film: a weaker elasticity could facilitate the liquid drainage. Consequently, the denaturation in this case is ought to decrease the lag time. In these runs, a significant stability loss is observed for the 80-3 product, while the NP and 70-3 cannot be clearly distinguished, maybe partly due to the nonlinearity of this effect.

Pressure Drop and Process Viscosity

The in-line viscosity is an important feature in the process development. A coarse approach is attempted here to target this property by the pressure drop measurement, by assuming a monophasic model. The pressure drop values for all the experiments are plotted versus the gas + liquid superficial velocity in Figure 20. They gather more or less on trend curves for various void fractions, what is explained by the first-order effect of the density in the pressure drop.

The pressure drop definition (Eq. 12) involves the physical properties of the foam, at first its density ρ_E, defined in Eq. 11, and second η_E, the apparent viscosity in the static mixer (or process viscosity).

$$\rho_E = \alpha\rho_{G,I} + (1-\alpha)\,\rho_L \tag{11}$$

$$\Delta P = \lambda \frac{L}{D_H}\frac{\rho_E U_E^2}{2} \tag{12}$$

In this equation, λ is the pressure drop factor expressed, in laminar regime, by Eq. 13

$$\lambda = \frac{Kp}{\mathrm{Re}} \tag{13}$$

where Reynolds number is defined by

$$\mathrm{Re} = \frac{\rho_E\, U_E\, D_H}{\eta_E} \tag{14}$$

Then, the process viscosity is computed as the ratio between the typical shear stress τ_a and the typical shear rate $\dot{\gamma}_a$ in the process, with

$$\dot{\gamma}_a = K_S \frac{U_E}{D} \tag{15}$$

$$\tau_a = \eta_E \quad \dot{\gamma}_a \tag{16}$$

By identifying the pressure drop in the momentum balance $\frac{\Delta P}{L} = \frac{4\tau_a}{D_H}$ with Eq. 12, the apparent viscosity can be computed

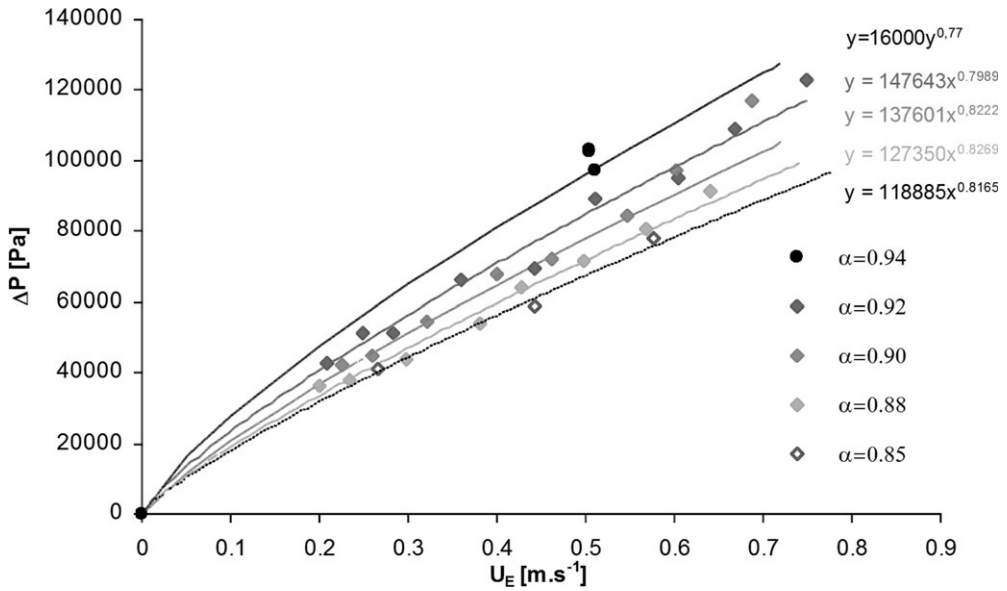

Figure 20. Pressure drop measurements and trend curves depending on the void fraction.

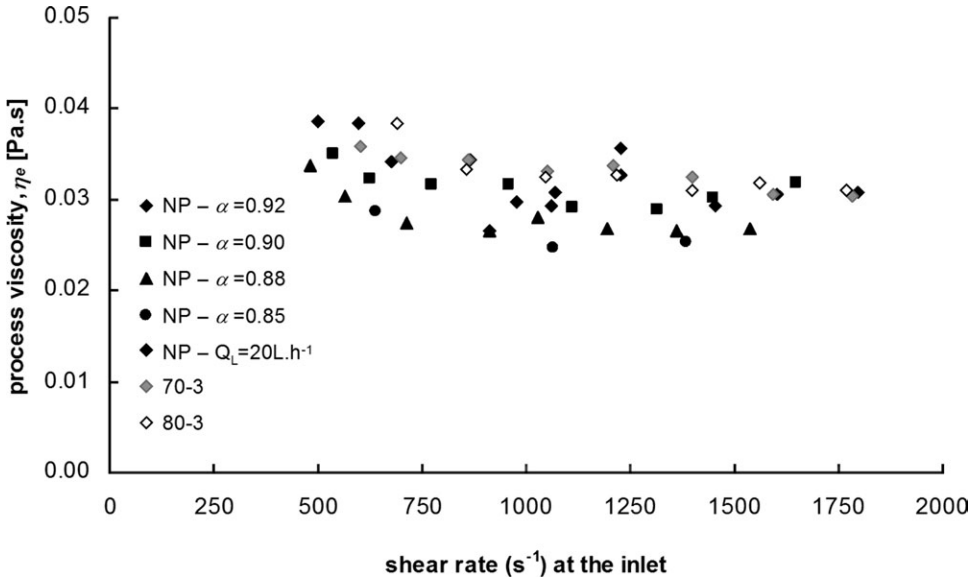

Figure 21. Foam apparent viscosity for the all runs.

with the K_p and K_s values of Li[35,42] and Bone[42] determined in the same geometry, which are $K_p = 1472$ and $K_s = 24$.

It can be observed on Figure 21 that the raw results are scattered when presented as function of the shear rate. This can be explained by the fact that the viscosity may depend on the foam structure besides the liquid phase nature. Hence, the trend of the viscosity is roughly assumed to be identical to that of the shear modulus, depending on both diameter and void fraction (cf the section entitled Effect of the structure on the foam end-used properties (only NP)). That leads to the definition of a "reduced viscosity" in Eq. 16 that should now mainly depend on the liquid nature

$$\eta_r = \frac{\eta_E}{d*^{0,6} \quad (1-\alpha)^{0,6}} \tag{17}$$

Indeed, in Figure 22, the reduced viscosity values match on power law trend curves, which mean that the main effects of the foam structure are taken into account by this model. The three products are slightly but clearly distinguished in this presentation, with the same ranking as for the shear modulus. This result could obviously be refined with a more appropriate model and a greater amount of experiments.

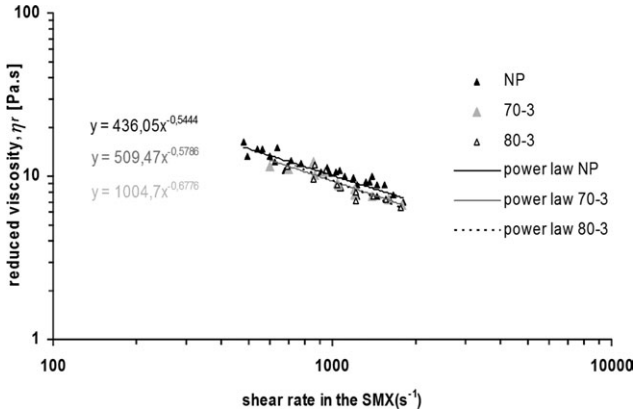

Figure 22. Foam reduced viscosity for all the runs.

Conclusion and Prospects

The SMX foaming process is suitable for the elaboration of foam with controlled structure. This is ensured by the complete mixing of the gas and the liquid flow rates, contrary to batch processes where the overrun depends on the liquid properties. This feature leads to interesting potentialities: (1) the possibility to investigate the structure influence on the foam end-used properties, especially the rheology and the stability, (2) the possibility to investigate the influence of the formulation for a given structure, (3) for practical purpose, the possibility to "correct" the effect of the formulation on the end-used properties by the structure: for instance to offset the loss of stability due to the protein denaturation by a smaller bubble diameter.

In this study dedicated to EWP foams, in a first step, we have specifically studied the structure influence of the foam—bubble size distribution and overrun—on its rheology and stability. In a second step, it is shown that in the range of our operating conditions, the EWP denaturation does not modify the foam structure, but significantly affects the rheology and the stability. The interfacial rheology, which is not directly involved in the bubble break-up, but in the "long time scales" interfacial film dynamics, seems to explain these differences in the end-used behavior.

We have demonstrated that this process is a versatile tool for both fundamental purposes of the liquid foams study, and industrial considerations about the foam properties mastering. Nevertheless, there is still a lack of knowledge in the process hydrodynamics to propose an accurate design at industrial scale. In this regard, there is a need of sizing criteria, which could be provided by a model based on a break-up model along the mixer. This approach will be proposed in a future work.

Acknowledgments

This program has been supported by a research grant of the French government (MENRT). The scientific purposes have been proposed by

the Adro-Ouest association of egg industries in the west of France. The technical support of Oniris-GPA, especially Luc Guihard and Christophe Couedel, are deeply acknowledged for the perfect implementation of the experimental rig. The authors gratefully thank Alain Riaublanc (INRA, Nantes) for the interfacial measurements.

Notation

EWP = egg white proteins
NP, 70-3, 80-3 = denaturation conditions (temperature-time table)
pdf = probability density function
D = pipe diameter, m
d^* = dimensionless diameter, −
D_H = SMX static mixer hydraulic diameter, m
D_m = modal diameter, m
DI = dispersion index of the bubble size distribution, −
$|G^*|_{1Hz}$ = viscoelastic modulus at the frequency of 1Hz, Pa
k = texture loss factor, %
L = SMX static mixer length, m
P = pressure, Pa
Q = volume flow rate, L h^{-1}
Q_m = mass flow rate, kg h^{-1}
Re = Reynolds number, −
S = SMX static mixer section, m^2
t_0 = drainage lag time, s
U = interstitial velocity in the mixer

Greek letters

α = void fraction, −
$\dot{\gamma}$ = shear rate, s^{-1}
ΔP = pressure drop between air injection and ambient, Pa
ε = SMX static mixer porosity, −
$|\varepsilon|_{0.01Hz}$ = interfacial extensional modulus at the frequency of 0.01 Hz, mN m^{-1}
η = viscosity, Pa s
λ = pressure drop factor, −
ρ = density, kg m^3
σ = surface tension, N m^{-1}
τ = shear stress, Pa

Subscripts

A, atm = at ambient
C = relative to the continuous phase or to the cell section
D = relative to the dispersed phase
E = relative to the in-line mixture gas + liquid
eq = equilibrium value
G = gas
I = relative to the injection section
L = liquid

Literature Cited

1. Campbell G, Mougeot E. Creation and characterisation of aerated food products. *Trends Food Sci Technol*. 1999;10:283–296.
2. Davis JP, Foegeding EA. Comparisons of the foaming and interfacial properties of whey protein isolate and egg white proteins. *Colloids Surf B*. 2007;54:200–210.
3. Kato A, Ibrahim HR, Watanabe H, Honma K, Kobayashi K. New approach to improve the gelling and surface functional properties of dried egg white by heating in dry state. *J Agric Food Chem*. 1989;37:433–437.
4. Kato A, Tanaka A, Matsudomi N, Kobayashi K. Deamidation of ovalbumin during S-ovalbumin conversion. *Agric Biol Chem*. 1986;50:2375–2376.
5. Kato A, Tsutsui N, Matsudomi N, Kobayashi K, Nakaï S. Effects of partial denaturation on surface properties of ovalbumin and lysozyme. *Agric Biol Chem*. 1981;45:2755–2760.
6. Rouimi S, Schorsch C, Valentini C, Vaslin S. Foam stability and interfacial properties of milk protein-surfactant systems. *Food Hydrocolloids*. 2005;19:467–478.
7. Stanley DW, Goff HD, Smith AK. Texture-structure relationships in foamed dairy emulsions. *Food Res Int*. 1995;29:1–13.
8. Boutonnier J-L. Crèmes glacées, glaces et sorbets: formulation et fabrication. *Techniques de l'ingénieur*. 2001;F8010:1–10.
9. Schorsch C. Formulation des mousses laitières. *Techniques de l'ingénieur*. 2007;J2268:1–11.
10. Balerin C, Aymard P, Ducept F, Vaslin S, Cuvelier G. Effect of formulation and processing factors on the properties of liquid foams. *J Food Eng*. 2007;78:802–809.
11. Hanselmann W, Windhab E. Flow characteristics and modelling of foam generation in a continuous rotor/stator mixer. *J Food Eng*. 1999;38:393–405.
12. Muller-Fischer N, Suppiger D, Windhab EJ. Impact of static pressure and volumetric energy input on the microstructure of food foam whipped in a rotor-stator device. *J Food Eng*. 2006;80:306–316.
13. Müller-Fischer N, Windhab EJ. Influence of process parameters on microstructure of food foam whipped in a rotor-stator device within a wide static pressure range. *Colloids Surf A*. 2005;263:353–362.
14. Vial C, Thakur RK, Djelveh G, Picgirard L. Continuous manufacturing of a light-textured foamed fresh cheese by dispersion of a gas phase. I. Influence of process parameters. *J Food Eng*. 2005;77:1–13.
15. Indrawati L, Narsimhan G. Characterisation of protein stabilized foam formed in a continuous shear mixing apparatus. *J Food Eng*. 2008;88:456–465.
16. Indrawati L, Wang Z, Narsimhan G, Gonzales J. Effect of processing parameters on foam formation using a continuous system with a mechanical whipper. *J Food Eng*. 2008;88:65–74.
17. Thakur RK, Vial C, Djelveh G. Influence of operating conditions and impeller design on the continuous manufacturing of food foams. *J Food Eng*. 2003;60:9–20.
18. Thakur RK, Vial C, Djelveh G. Foaming of commercial grade food products in a continuous stirred column. *Trans IChemE, PartA*. 2003;81:1083–1089.
19. Thakur RK, Vial C, Djelveh G. Combined effects of process parameters and composition on foaming of dairy emulsions at low temperature in an agitated column. *J Food Eng*. 2005;68:335–347.
20. Thakur RK, Vial C, Djelveh G. Effect of composition and process parameters on elasticity and solidity of foamed food. *Chem Eng Process*. 2008;47:474–483.
21. Baker JR. Motionless mixers stir up new uses. *Chem Eng Prog*. 1991;87:32–38.
22. Cybulski A, Werner K. Static mixers—criteria for applications and selection. *Int Chem Eng*. 1986;26:171–180.
23. Thakur RK, Vial C, Nigam KDP, Nauman EB, Djelveh G. Static mixers in the process industries—a review. *Trans IChemE, Part A*. 2003;81:787–826.
24. Al Taweel AM, Chen C. A novel static mixer for the effective dispersion of immiscible liquids. *Trans IChemE*. 1996;74:445–450.
25. Al Taweel AM, Walker LD. Liquid dispersion in static in-line mixers. *Can J Chem Eng*. 1983;61:527–533.
26. El-Jaby U, Cunningham M, McKenna TFL. Continuous production of miniemulsions using in-line SMX elements. *AIChE J*. 2011;57:1585–1594.
27. Legrand J, Morançais P, Carnelle G. Liquid-liquid dispersion in an SMX-SULZER static mixer. *Trans IChemE*. 2001;79:949–956.
28. Streiff F. New fundamentals for liquid-liquid dispersion using static mixers. In: 9th European Conference on Mixing. Vol. 11. Paris, France: Récents Progrès en Génie des Procédés. Lavoisier. Tec Doc, 1997.
29. Al Taweel AM, Yan J, Azizi F, Odedra D, Gomaa HG. Using in-line static mixers to intensify gas-liquid mass transfer processes. *Chem Eng Sci*. 2005;60:6378–6390.
30. Couvert A, Sanchez C, Charron I, Laplanche A, Renner C. Static mixers with a gas continuous phase. *Chem Eng Sci*. 2006;61:3429–3434.
31. Fradette L, Li H-Z, Choplin L, Tanguy P. Gas/liquid dispersions with a SMX static mixer in the laminar regime. *Chem Eng Sci*. 2006;61:3506–3518.
32. Heyouni A, Roustan M, Do-Quang Z. Hydrodynamics and mass transfer in gas-liquid flow through static mixers. *Chem Eng Sci*. 2002;57:3325–3333.
33. Shah NF, Kale DD. Two-phase, gas-liquid flows in static mixers. *AIChE J*. 1992;38:308–310.
34. Germain E, Streiff FA, Juvet JE. Les mélangeurs statiques, des réacteurs simples et efficaces. *Informations Chim*. 1996;371:141–147.
35. Li HZ, Fasol C, Choplin L. Hydrodynamics and heat transfer of rheologically complex fluids in a Sulzer SMX static mixer. *Chem Eng Sci*. 1996;51:1947–1955.
36. Mutsakis M, Streiff FA, Schneider G. Advances in static mixing technology. *Chem Eng Prog*. 1986:42–48.
37. Talansier E. *PhD Thesis. Etude du foisonnement par mélangeur statique appliqué à la structuration des mousses de blanc d'oeuf*

dénaturé par traitement thermique. Nantes, France: Faculté des sciences et des techniques, Université de Nantes, 2009.

38. Talansier E, Loisel C, Dellavalle D, Lechevalier V, Legrand J. Optimization of dry heat treatment of egg white in relation to foam and interfacial properties. *LWT—Food Sci Technol*. 2009;42:496–503.
39. Beverung CJ, Radke CJ, Blanch HW. Protein adsorption at the oil/water interface: characterization of adsorption kinetics by dynamic interfacial tension measurements. *Biophys Chem*. 1999;81:59–80.
40. Benjamins J, Cagna A, Lucassen-Reynders EH. Viscoelastic properties of triacylglycerol/water interfaces covered by proteins. *Colloids ans Surfaces A*. 1996;114:245–254.
41. Mahmoudi N, Gaillard C, Boué F, Axelos M, Riaublanc A. Self-Similar assemblies of globular whey proteins at the air-water interface: Effect of the structure. *J Colloid Interface Sci*. 2010;345:54–63.
42. Bone S. *PhD Thesis. Etude d'un procédé de fabrication de microcapsules par émulsification dans un mélangeur statique*. Nantes, France: Faculté des sciences et des techniques, Université de Nantes 2005.
43. Vigneau E, Loisel C, Devaux MF, Cantoni P. Number of particles for the determination of size distribution from microscopic images. *Powder Technol*. 2000;107:243–250.
44. Marze SPL, Saint-Jalmes A, Langevin D. Protein and surfactant foams: linear rheology and dilatancy effect. *Colloids Surfaces A*. 2005;263:121–128.

Manuscript received Apr. 19, 2011, and revision received Mar. 3, 2012.